ZART: A Novel Multiresolution Reconstruction Algorithm with Motion-blur Correction for Single Particle Analysis

D. Herreros [1]*, **J. Kiska** [2], **E. Ramírez-Aportela** [1], **J. Filipovic** [2], **J. M. Carazo** [1]* and **C. O. S. Sorzano** [1]*

1 - *Centro Nacional de Biotecnologia-CSIC,* C/ Darwin, 3, 28049, Cantoblanco, Madrid, Spain
2 - *Institute of Computer Science,* Masaryk University, Botanická 68a, 60200 Brno, Czech Republic

Correspondence to D. Herreros, J.M. Carazo and C.O.S. Sorzano: dherreros@cnb.csic.es *(D. Herreros),* carazo@cnb.csic.es *(J.M. Carazo),* coss@cnb.csic.es *(C.O.S. Sorzano)@HerosCGM, @InstructI2PC* 🐦 *(D. Herreros)*
https://doi.org/10.1016/j.jmb.2023.168088
Edited by Fei Sun

Abstract

One of the main purposes of CryoEM Single Particle Analysis is to reconstruct the three-dimensional structure of a macromolecule thanks to the acquisition of many particle images representing different poses of the sample. By estimating the orientation of each projected particle, it is possible to recover the underlying 3D volume by multiple 3D reconstruction methods, usually working either in Fourier or in real space. However, the reconstruction from the projected images works under the assumption that all particles in the dataset correspond to the same conformation of the macromolecule. Although this requisite holds for some macromolecules, it is not true for flexible specimens, leading to motion-induced artefacts in the reconstructed CryoEM maps. In this work, we introduce a new Algebraic Reconstruction Technique called ZART, which is able to include continuous flexibility information during the reconstruction process to improve local resolution and reduce motion blurring. The conformational changes are modelled through Zernike3D polynomials. Our implementation allows for a multiresolution description of the macromolecule adapting itself to the local resolution of the reconstructed map. In addition, ZART has also proven to be a useful algorithm in cases where flexibility is not so dominant, as it improves the overall aspect of the reconstructed maps by improving their local and global resolution.

Introduction

CryoEM SPA[1] has proven to be one of the most successful techniques to recover the structure of a macromolecule at near-atomic resolution. In addition, its ability to capture different macromolecular states is driving the CryoEM field towards a new way of analyzing and understanding macromolecular flexibility.

However, the reconstruction of structures at high resolution is compromised when the sample is heterogeneous, as the reconstruction algorithms assume that all particles involved in the reconstruction process are compatible with a single underlying 3D map. To overcome the current challenges arising with heterogeneous datasets, it is possible to take advantage of 3D classifications[2] to isolate the particles belonging to a given conformation to improve the resolution of the reconstruction. Nevertheless, the classification process will decrease the number of particles that are available to reconstruct a given conformation, compromising again the maximum resolution achievable. In addition, new methods specifically

developed to estimate richer conformational landscapes are also appearing in the field.[3–8] However, these algorithms focus on the estimation of new conformational states, but they do not take advantage of the estimated heterogeneity information to further improve the resolution in those areas exhibiting larger degrees of flexibility.

In this work, we propose a novel reconstruction algorithm called ZART (Zernike3D-based Algebraic Reconstruction Technique), an ART-based[1] [9] multiresolution reconstruction method able to take advantage of the estimated per-particle continuous heterogeneity computed by the Zernike3D algorithm to correct particle inhomogeneities.[10] Thanks to the previous correction, it is possible to improve the local resolution of the reconstructions. Additionally, ZART has been designed to improve the features of the final maps even if motion corrections are not considered, helping with the tracing of the map to achieve better structures. Finally, a multiresolution approach has been adopted to adapt the local complexity of the reconstructed map to the estimated local resolution.

Compared to the first implementation of ZART presented in,[10] this work proposes a major change in the algorithm, allowing to reconstruct heterogeneity corrected maps even if the Zernike3D information was estimated in particles with a larger sampling rate. Also, in our previous implementation, the reconstruction sampling rate was restricted to the particles' sampling rate used during the landscape estimation, thus compromising the maximum resolution possible. Now, we have dropped this constraint as we are able to adapt the Zernike3D coefficients to any pixel size of interest.

In addition, the multiresolution reconstruction mode of ZART is also introduced, which provides a new approach to further improve the quality of the reconstructions compared to the previous implementation.

Results

SARS-CoV-2 spike phantom reconstruction

The main objective of the following results is to analyze the characteristics of ZART through the reconstruction of a synthetic dataset. To that end, we simulated a SARS-CoV-2 Coulomb potential map using the EASFs[2] [11] from the PDB 6VSB.[12] The map was then projected to generate a gallery of 18,309 images with a sampling rate 2.40 Å/px. The motivation behind downsampling the images is to get a dataset where the sharpening effect of ZART can be more easily assessed. It is worth mentioning that the images were not further processed to include noise or the CTF[3] of the microscope. Our aim at this moment is to produce an ideal dataset that allows

characterizing ZART capabilities in optimal conditions. Later in the article, we will use experimental data in which noise and CTF are naturally present.

We compared the reconstructions by ZART and Fourier gridding[13] as implemented in Xmipp.[14] The resulting maps are shown in Figure 1(a) and Figure 1(b). As can be seen from the 3D volumes and the slices, ZART yields a reconstruction with finer details, simplifying the interpretation of the map features compared to a standard Fourier reconstruction.

Since the simulated particles constitute an ideal homogeneous dataset, no motion correction was applied during the reconstruction of the ZART map. Therefore, the main reason behind the improvement in the features of the map comes from the deconvolution with a Gaussian implied by our method. This idea is further discussed in Section 'Zernike3D Algebraic Reconstruction Technique'.

In addition to the evaluation of the quality of the reconstructions, Figure 1(c) also includes the convergence curve extracted from the reconstruction error computed during the first iteration of the ZART algorithm for every image. The plot shows that a meaningful reconstruction (in terms of convergence) can be achieved after processing 5000 images from the original phantom dataset. However, it is important to note that the convergence speed has a strong dependence on the relaxation factor chosen to reconstruct a given dataset. A more detailed discussion of the importance of the relaxation factor in the reconstruction process is available in Section 'Zernike3D Algebraic Reconstruction Technique'.

Figure 2 shows a more detailed comparison of the reconstructed Fourier and ZART maps against the structure used to generate the phantom data. Thanks to the intrinsic sharpening of ZART, the reconstructed map is able to define better the local features present in the spike atomic structure.

Arabinofuranosyltransferase reconstruction

In order to assess the performance of our ZART reconstruction algorithm on a more realistic scenario, the dataset EMPIAR-10391 was used for this task.[15] This dataset was processed inside Scipion following a complete workflow to extract a complete particle set of 35 k images with a sampling rate 1.06 Å/px. The alignment and CTF information associated with the particles was estimated with Relion.[16]

The particles were afterwards reconstructed with Relion and ZART and in all cases sharpened with 3DEMhancer.[18] In the case of ZART, we followed three different reconstruction approximations: a standard reconstruction and two multiresolution reconstructions with $M = 3$ and $M = 6$ multiresolution levels respectively. Heterogeneity correction was not applied in this cases in order to compare

---

1 Algebraic Reconstruction Technique.
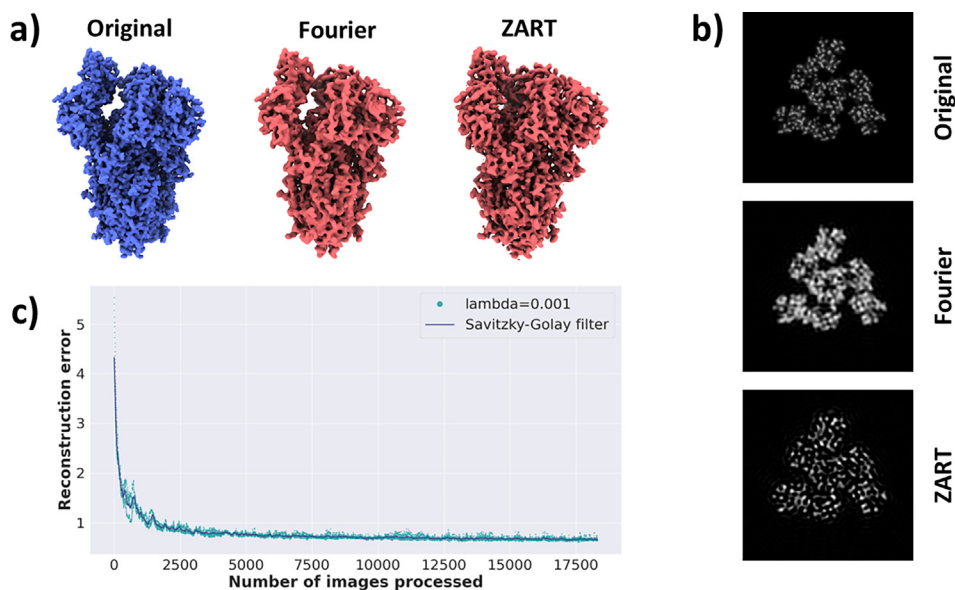2 Electron Atomic Scattering Factors.
3 Contrast Transfer Function.

Figure 1. Results obtained for the comparison of ZART and Fourier-based reconstruction for the SARS-CoV-2 spike phantom images. (a) shows the original phantom simulated from PDB 6VSB, and the Fourier and ZART reconstruction from the phantom images. The map comparison shows that ZART provides a sharper representation of the different features of the spike. (b) shows some slices of the maps represented in a). Similarly to the conclusion drawn from the maps, ZART provides a sharper representation of the features compared to Fourier, providing a more meaningful representation. (c) shows the convergence curve of ZART during the first iteration of the algorithm. As can be seen from the curve, around 5000 images are needed to be processed to get a meaningful reconstruction in terms of convergence. Together with the original scatter data, the Savitzky–Golay filtered curve is also provided to aid in the visualization of the plot.
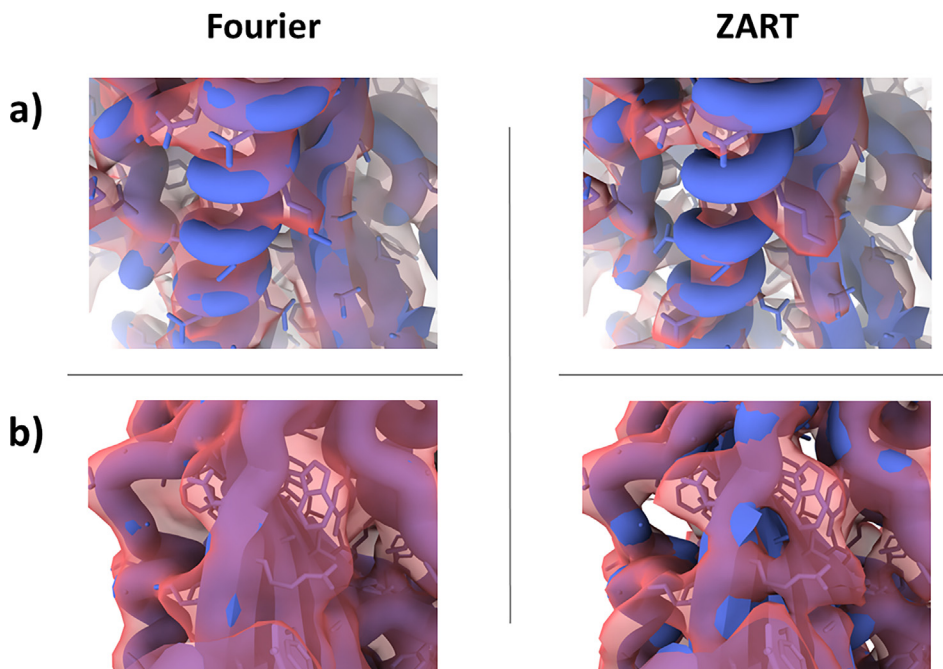

Figure 2. Comparison of Fourier and ZART reconstructions against the atomic structure 6VSB used to simulate the phantom particles. Thanks to the intrinsic sharpening characteristics of ZART, the reconstruction is able to define more accurately different areas of the map. The panels were generated with ChimeraX software,[17] and histogram thresholds were set to 0.388 and 0.209 for Fourier and ZART respectively.

more effectively the standard and multiresolution reconstruction modes. The resulting reconstructed maps are shown in Figure 3(a). The colormap represents the local resolution estimation in Angstroms for each voxel, computed with MonoRes.[19] As can be seen from the maps and their corresponding local resolutions, ZART provides a reconstruction with improved local resolution and better features compared to the Relion reconstruction.

In order to provide a more quantitative comparison of the maps, the local resolution histograms computed with MonoRes were also compared. Figure 3(b) shows the comparison of the resolution histogram of Relion and ZART multiresolution map with $M = 6$ resolution levels. As can be seen from the histograms, ZART pushes a larger number of voxels towards the

high-resolution regime in the range of 2.5 Å–3.2 Å. Thanks to this push, the average of the local resolutions improves from 7.0 Å to 4.0 Å.

We also computed the FSC curves of all the reconstructions analyzed during this section. The resulting curves are shown in Figure 3(c). It can be noted that ZART also improves the global resolution of the map from 3.3 Å to 3 Å. This implies an improvement of 0.3 Å due to ZART and of 0.5 Å compared to the reported resolution of the originally published maps, thanks in this latter case of the quality of the complete workflow used in this work.

Another effect that can be observed when comparing the standard and multiresolution reconstructions in ZART is that multiresolution can further improve the local resolution histograms of
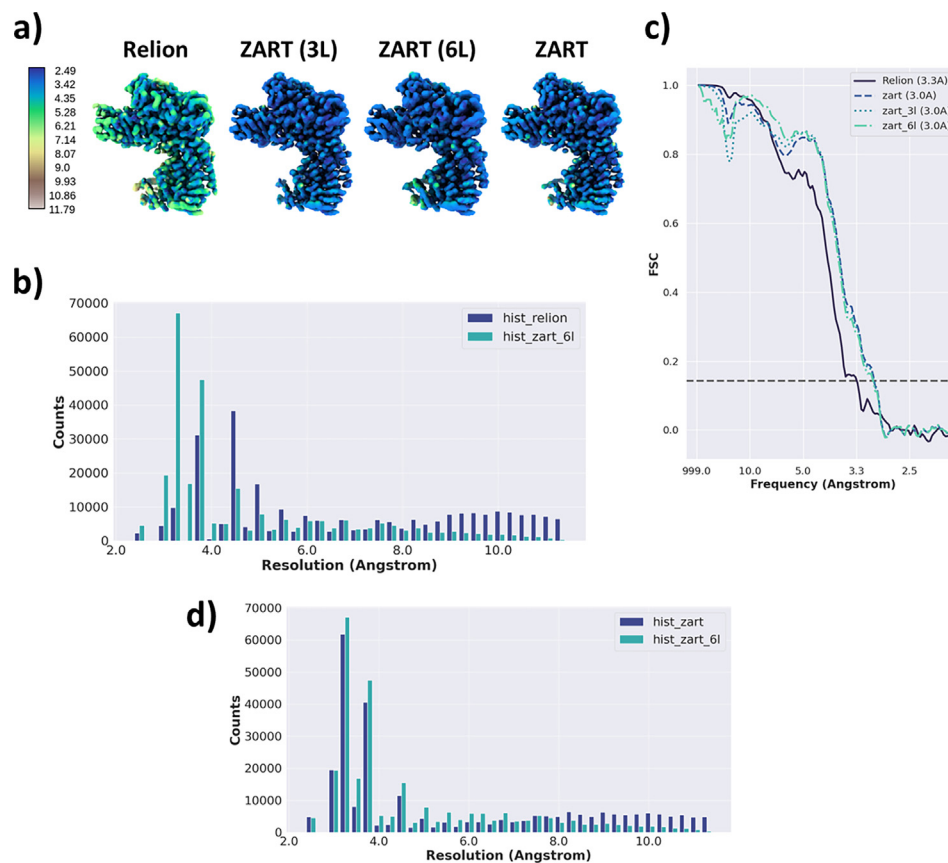

Figure 3. Reconstructions of the Arabinofuranosyltransferase from the EMPIAR-10391 dataset. (a) shows a comparison of the Relion and ZART reconstructions sharpened by DeepEMhancer[18] software. In the case of ZART, we perform two multiresolution reconstructions with 3 and 6 levels respectively and a standard reconstruction without multiresolution. The map comparison suggests that ZART provides a sharper representation with improved local resolution. However, this is difficult to appreciate directly on these small representations and for that, we are making a quantitative assessment in other panels of this Figure. Panel (b) shows the local resolution histograms of the maps shown in (a) computed with MonoRes.[19] The histograms show that ZART pushes a large number of voxels towards the high-resolution regime. (c) shows the FSC curves of the maps shown in (a). As shown in the previous panels, our new reconstruction method pushes the overall resolution of the map around 0.3 Å. (d) Comparison of the local resolution between the ZART reconstructions both in standard and in multiresolution mode. The comparison shows that multiresolution supposes a little improvement in the local resolution values thanks to the consideration of multiresolution grids with variable Gaussian widths.

the reconstructed volumes, although the difference is small. Figure 3(d) shows the comparison of the local resolution histograms between the final reconstruction of ZART (in standard mode) and the ZART in multiresolution mode (with 6 multiresolution levels). The two histograms show a similar type of distribution of the local resolutions, although multiresolution pushes a larger amount of values towards the high-resolution regime. In addition, multiresolution implementation has little impact on the performance of every reconstruction iteration, allowing to achieve maps in a similar time compared to the standard reconstruction mode.

Figure 4 shows a more detailed comparison of the Relion and ZART reconstructions against the original structure published with the dataset. In order to make the comparison more reliable, the structural model has not been further refined against any of the two previous maps, and no sharpening was applied to the volumes. The result illustrates how the sharpening applied by ZART leads to a reconstruction representing more accurately the features of the arabinofuranosyltransferase.

Additionally, a comparison of ZART with CryoSPARC non-uniform refinement was performed, in order to better assess the performance against other algorithms applying a de-blur to the resulting map. The results are provided in Figure 5. Overall, both CryoSPARC and ZART maps show similar features, although for some regions ZART showed a better definition of the molecular structure. We also provide a comparison of the local resolution histograms associated with the two previous reconstructions, together with some measurements drawn from them in Supplementary Figure 1.

P. falciparum 80S ribosome reconstruction

The *P. falciparum* 80S ribosome of EMPIAR-10028[20] has become a quite standard dataset to evaluate the performance and accuracy of continuous heterogeneity algorithms, due to the presence of significant conformational changes that can be extracted directly at particle level.
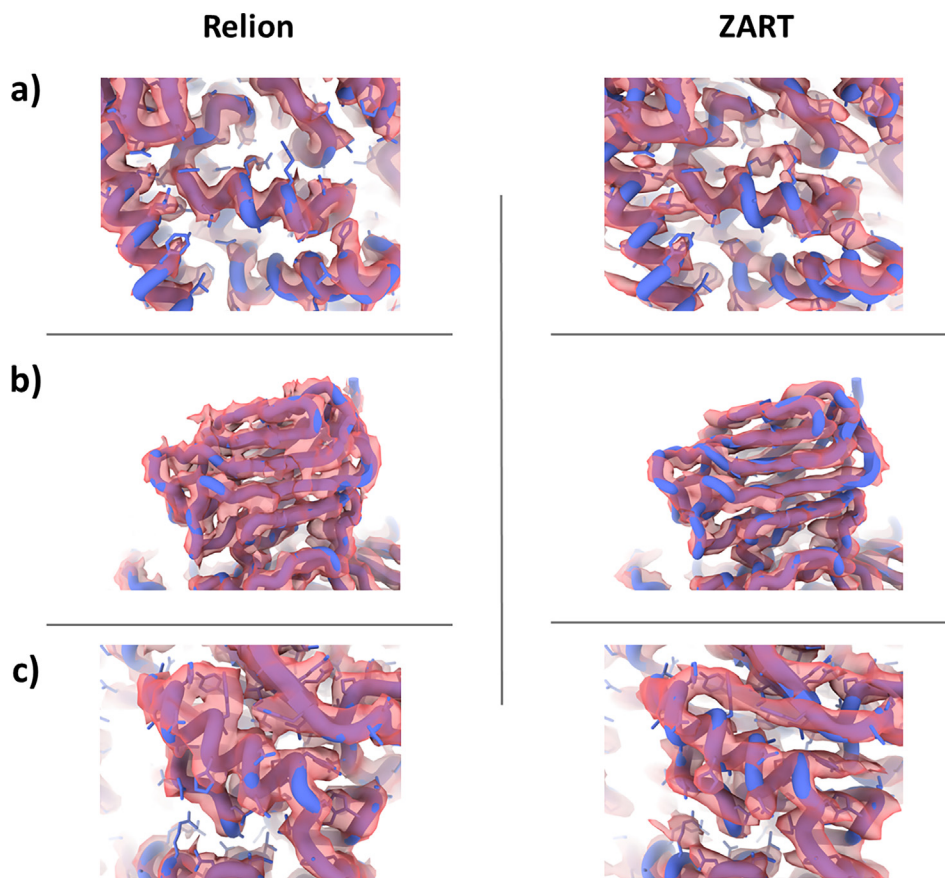

Figure 4. Comparison of Relion and ZART reconstructions (without sharpening) against the original atomic structure published with the EMPIAR-10391 dataset (PDB entry 6WBX). Thanks to the intrinsic sharpening characteristics of ZART, the reconstruction is able to better define different map regions at similar map thresholds. The panels were generated with ChimeraX software,[17] and histogram thresholds were set to 0.012 and 0.255 for Relion and ZART respectively.
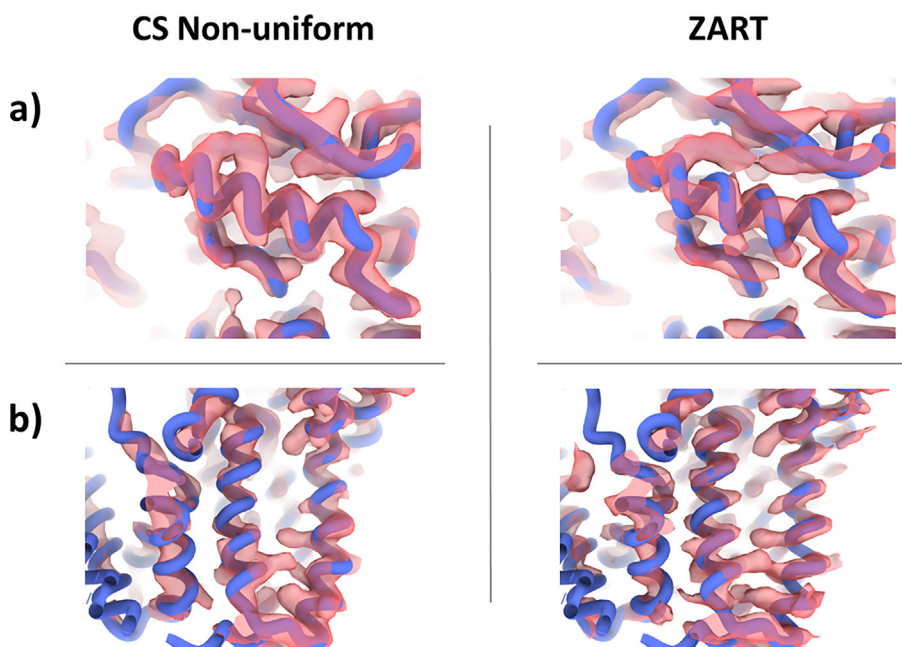
CS Non-uniform   **ZART**

Figure 5. Comparison of CryoSPARC non-uniform refinement and ZART reconstructions (without sharpening) against the original atomic structure published with the EMPIAR-10391 dataset (PDB entry 6WBX). The comparison shows that the de-blurring applied by the two algorithms leads to similar results, although ZART is able to define better some structural features. The panels were generated with ChimeraX software,[17] and histogram thresholds were set to 0.85 and 0.255 for CryoSPARC and ZART respectively.

Therefore, we decided to evaluate the ability of ZART to revert conformational changes and improve motion-blurred areas with the EMPIAR-10028 dataset. To that end, we processed the submitted data inside Scipion to get a set 50 k particles with CTF and alignment information. Both, the alignment and CTF were estimated with CryoSPARC[21] in two independent runs, followed by a consensus step[22] to improve the accuracy of the measurements. The sampling rate of the images fed to the reconstruction algorithms was 1.34 Å/px.

We estimated the per-particle conformational changes with the Zernike3D algorithm.[10] This method relies on a mathematical basis able to express a deformation field that can be used to approximate any particle conformation in 3D at the level of CryoEM maps or atomic structures.

In this example, the estimated deformation fields are considered during the reconstruction process to reduce the structural differences among the particles and reduce motion blur artefacts. The application of the deformation field compensation can be done either using the standard ZART reconstruction algorithm or its multiresolution version. However, in this case, and with the aim of reducing the number of parametric choices and concentrating only on the differences due to motion correction, the reconstruction of the ribosome was done using standard ZART.

The comparison of the map reconstructed with CryoSPARC[21] and ZART with motion correction is provided in Figure 6(a). The maps were coloured according to their local resolution value estimated with MonoRes. As can be seen from the results, ZART provides better features (mostly on moving regions, such as the small subunit of the ribosome) thanks to the per-particle structural corrections.

Figure 6(b) shows the comparison of the local resolution histograms computed with MonoRes. Similarly to the results offered in the previous section, the application of ZART with motion correction increases the resolution of a larger number of voxels, mainly in the range from 3.0 Å to 4.5 Å. The average of the local resolution is also improved from 5.5 Å to 5.2 Å. The comparison of the FSC curves is also provided in Figure 6(c). In this case, ZART pushes the FSC around 0.1 Å.

Figure 7 shows a more detailed comparison of the differences between the CryoSPARC and ZART reconstructions in regions of high flexibility. The figure shows the comparison of the CryoSPARC and ZART reconstructions against the original structural model published together with the dataset. The structural model has not been further refined considering any of the two maps to simplify the comparison. Thanks to the correction of the ribosome motions, ZART is able to define better different features in flexible regions such as
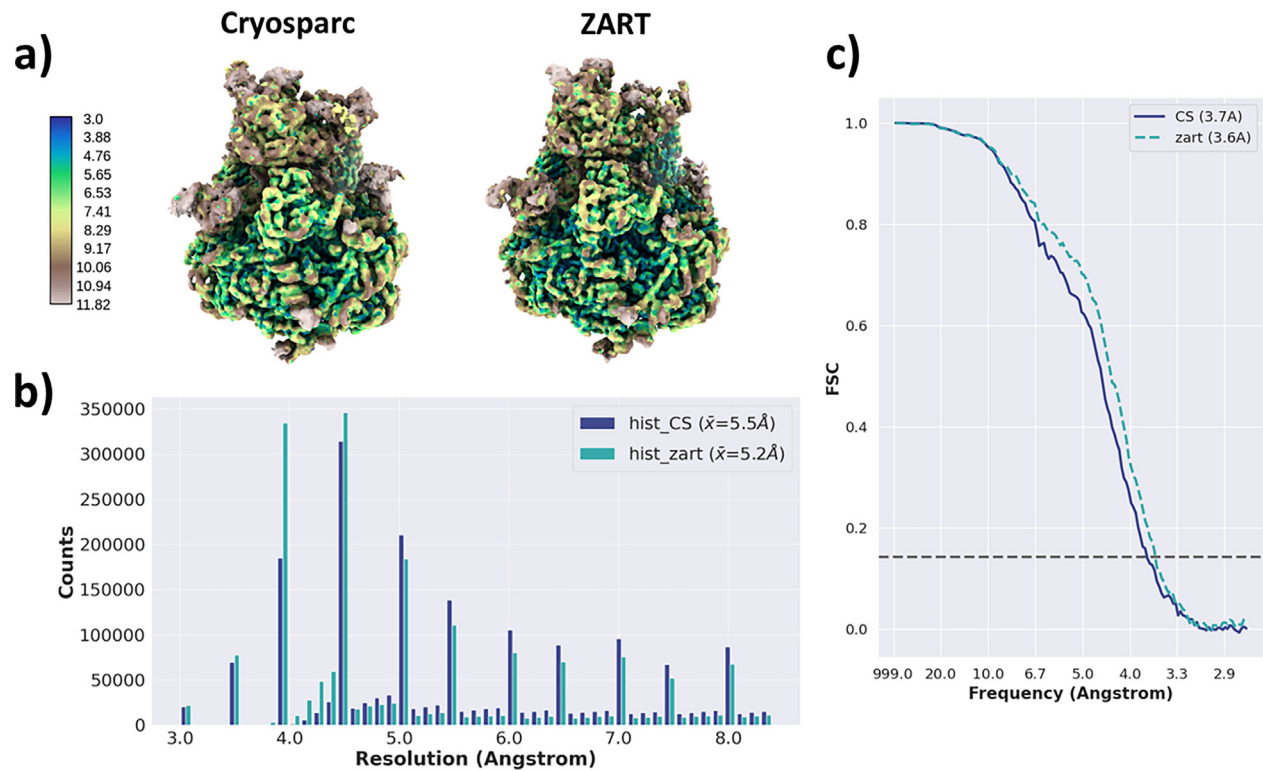
Figure 6. Comparison of ZART and CryoSPARC reconstructions for the *P. falciparum* 80S ribosome from EMPIAR-10028 dataset. (a) shows a comparison of the Cryosparc and ZART reconstructions sharpened by DeepEMhancer[18] software. In the case of ZART, we perform a standard reconstruction with no multiresolution, but correcting the motion blur artefacts thanks to the Zernike3D deformation fields computed for each particle in the dataset. The map comparison shows that ZART provides a sharper representation with improved local resolution. (b) shows the local resolution histograms of the maps in (a) computed with MonoRes.[19] The histograms show that ZART pushes a large number of voxels towards the high-resolution regime, being most of the voxels at the range 3.0 Å–4.5 Å. (c) shows the FSC curves of the maps shown in (a). For this case, ZART improves the overall resolution of the map by around 0.1 Å.
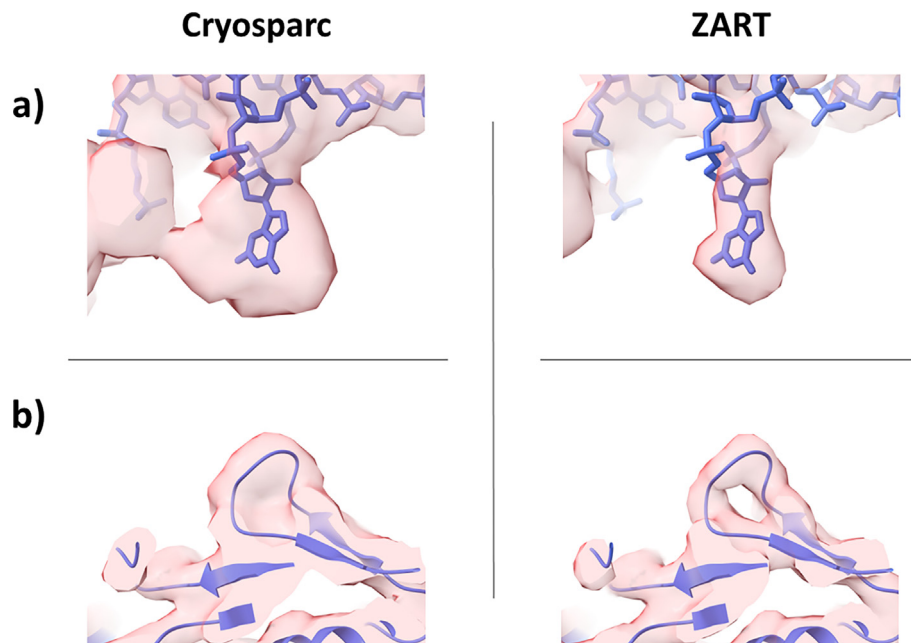

Figure 7. Comparison of CryoSPARC and ZART reconstructions (with motion blur correction) against the original atomic structure published with the EMPIAR-10028 dataset (PDB entries 3J79 and 3J7A). Thanks to the correction of each particle conformation during the reconstruction, ZART is able to define better the features usually hidden due to motion blur artefacts. The panels were generated with ChimeraX software.[17]
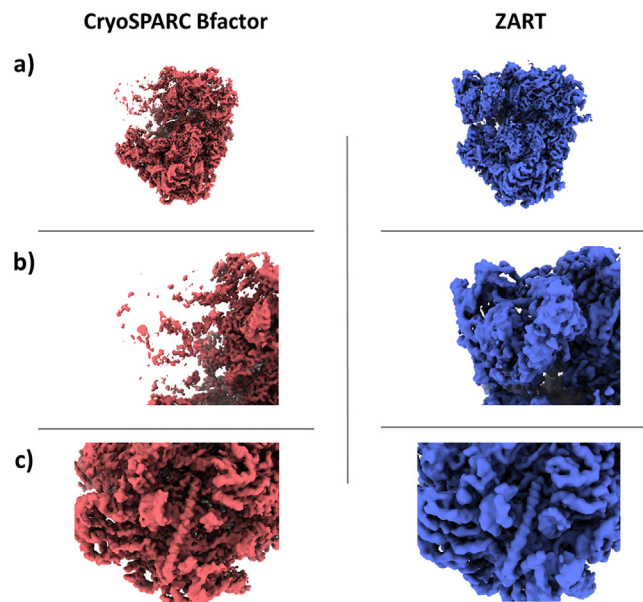
CryoSPARC Bfactor   **ZART**

Figure 8. Comparison of Bfactor corrected CryoSPARC reconstruction and ZART reconstructions (with motion blur correction). Both maps were post-process with DeepEMHancer[18] software in order to decrease the noise of the maps and improve the interpretability of the results. The Bfactor correction applied to the Relion reconstruction enhances the features located mostly on the core of the ribosome as observed in (c) compared to ZART. However, flexible regions are not properly recovered, being lost due to their low SNR as shown in (a) and (b). In contrast, ZART motion correction helps reducing the motion blur induced by the molecular motions, thus yielding a more complete map even after applying its intrinsic sharpening and DeepEMHancer. The panels were generated with ChimeraX software.[17]

Table 1 Execution times for the ZART algorithm (note that the standard ZART version has been the one used for this reporting). N and M are the parameters defining the size of the Zernike3D base. We show the performance for $N = 3$ and $M = 2$, which corresponds to our most common choice of parameters when estimating deformation fields, and also the one for $N=-$ and $M=-$, which refers to the case when no motion correction is considered during the reconstruction. We observe that for one million particles of size 300x300 pixels the time goes from three-quarters of an hour to an hour and a half, depending on whether we consider or not the deformation field correction (on a powerful CPU server, the GPU version is still under development).

Performance metrics for ZART algorithm			
Image size	N	M	Iteration time 10^6 particles (hours - 150 threads)
300	3	2	1.407
300	-	-	0.746

loops and key residues, as shown in the figure, producing information that can now be used to further refine the traced structural model starting from the ZART map, leading to better results.

We also provide a more in-depth comparison of the signal of different map slices in Supplementary Figure 2. As can be seen from the slice comparison, ZART provides a better representation of the features in the map, including the small subunit of the ribosome thanks to the heterogeneity correction coming from the Zernike3D deformation fields. Negative values have been excluded from the slices of CryoSparc and ZART to enhance the visualization of the protein signal.

In addition, ZART reconstruction was compared against the previous CryoSPARC map after

applying a Bfactor to better assess the intrinsic sharpening capabilities of ZART against other sharpening methods. In addition, both ZART and CryoSPARC Bfactor-corrected maps were post-process with DeepEMHancer using wide target mode, in order to decrease the noise of the reconstruction while keeping as reliably as possible the original information of the volumes.

The comparison is provided in Figure 8. The application of the Bfactor improves the quality of the ribosome core features, as this region is more rigid. However, the low SNR of the high-flexibility regions prevents them from being recovered appropriately after the Bfactor correction.

In contrast, the motion correction applied by ZART provides a better definition of the moving regions in the ribosome, which are properly

recovered even after applying the intrinsic sharpening of ZART and DeepEMHancer.

Table 1 provides some metrics about the computational performance of ZART.

Conclusions

We have introduced a new ART-based reconstruction method called ZART in this manuscript. Thanks to the modification in the interpolation scheme and volume recovery process, ZART is able to improve the local resolution of the reconstructed maps, without the need to further modify or refine the alignment and CTF information of the input particles.

Moreover, ZART can also create a map where the estimated Zernike3D deformation field per particle can be compensated for, or computationally "reverted", thus reducing motion blurring during the reconstruction and increasing the resolution of very flexible areas in the macromolecule. Compared to the implementation introduced in,[10] ZART reconstructions are no longer limited to the sampling rates used during the estimation of conformational landscapes. Therefore, is now possible to correct the heterogeneity-induced blurring of maps without compromising resolution, allowing ZART to reach high-resolution heterogeneity-corrected maps.

In addition, in this work we described the ZART multiresolution reconstruction approach, which takes advantage of the local resolution estimation of the maps reconstructed every two iterations to determine the resolution that should be used to further update different regions of the map. Multiresolution has proven to be a useful approach, as it leads to high-quality results without the need for so many ZART iterations, reducing the execution times compared to the initial implementation introduced in.[10] Finally, a multiresolution approach has intrinsically the potential to be less prone to be trapped in local minima.[23] Although we have not observed this effect in the cases presented in this work, these characteristics remain to be further explored in other data sets.

Methods

The Algebraic Reconstruction Technique

We express the reconstructed map in a series expansion with a basis function $b(\mathbf{r})$:

$$V(\mathbf{r}) = \sum_j x_j b\left(\frac{\mathbf{r} - \mathbf{r}_j}{\sigma}\right) \tag{1}$$

where $\mathbf{r}$ is a coordinate in the 3D space, $\mathbf{r}_j$ represents the location of the j-th basis function and σ its scale. The basis functions chosen are Gaussian functions. If all sigmas are equal, then the expression above can be expressed as a convolution.

$$V(\mathbf{r}) = \left(\sum_j x_j \delta(\mathbf{r} - \mathbf{r}_j)\right) \star b\left(\frac{\mathbf{r}}{\sigma}\right) \tag{2}$$

These Gaussians are distributed in a regular, rectangular grid with a step of σ pixels. Our motivation for this choice is that Gaussians can approximate a partition of unity with a very low error[24] when the spacing between two Gaussians is equal to their standard deviation. Partition of unity is an important property of basis functions that guarantees that they can reproduce any Sobolev function of the space W^2 (that is, sufficiently smooth, square-integrable functions). Additionally, Gaussians are spherically symmetric and their projection does not depend on the projection direction, making them very computationally efficient.

The projection of this volume onto an image is modelled as the line integral of this map. The projection direction and the in-plane shift are given by an Euler matrix, E, that acts on the spatial coordinates.[25] We define the auxiliary matrix H_t that will help to transform the 2D coordinate of the image into a 3D coordinate of the volume and will also help to perform the line integral as

$$\widetilde{H}_t^T = \begin{pmatrix} 1 & 0 & 0 \\ 0 & 1 & 0 \\ 0 & 0 & t \end{pmatrix} \tag{3}$$

Then, the projection is given by

$$\begin{aligned} I(\mathbf{s}) &= \int V\left(E^{-1}\widetilde{H}_t^T\mathbf{s}\right) dt \\ &= \int \left(\sum_j x_j b\left(\frac{E^{-1}\widetilde{H}_t^T\tilde{\mathbf{s}} - \mathbf{r}_j}{\sigma}\right)\right) dt \\ &= \sum_j x_j \int \left(b\left(\frac{E^{-1}\widetilde{H}_t^T\tilde{\mathbf{s}} - \mathbf{r}_j}{\sigma}\right)\right) dt \end{aligned} \tag{4}$$

Tildes above represent homogeneous coordinates.

The projection of a 3D Gaussian is a 2D Gaussian of the same σ. Let us refer to the 2D Gaussian as G. Then, the projection above can be simplified to

$$I(\mathbf{s}) = \sum_j x_j G\left(\frac{\mathbf{s} - E\mathbf{r}_j}{\sigma}\right) \tag{5}$$

If there is an in-plane shift, $\mathbf{s}_0$, then the model above has to be modified to

$$I(\mathbf{s}) = \sum_j x_j G\left(\frac{(\mathbf{s} - \mathbf{s}_0) - E\mathbf{r}_j}{\sigma}\right) \tag{6}$$

For a particular pixel $\mathbf{s}_i$ we will have

$$I(\mathbf{s}_i) = \sum_j x_j G\left(\frac{(\mathbf{s}_i - \mathbf{s}_0) - E\mathbf{r}_j}{\sigma}\right) = \sum_j x_j a_{E,\mathbf{s}_0,ij} \tag{7}$$

where the coefficient $a_{E,\mathbf{s}_0,ij}$ represents the projection of the j-th basis of the volume onto the i-th pixel of the image whose alignment parameters are given by the matrix $\widetilde{E}$ and the in-plane shift $\mathbf{s}_0$.

We may collect all experimental images into a single vector, $\mathbf{I}$, and construct the corresponding

matrix, A, with all the matrices for the individual projections. Then, the reconstruction problem boils down to solve a linear equation system of the form

$$A\mathbf{x} = \mathbf{I} \qquad (8)$$

Among the possible algorithms to solve this equation system, we have chosen Block-ART as it provides a good balance between computational complexity and convergence speed.[9]

The 3D reconstruction process starts with an initial solution, $\mathbf{x}^{(0)}$, typically an empty vector of zeroes. Then, it iterates over the different experimental images and updates the k-th estimate of the 3D reconstruction according to

$$\mathbf{x}^{(k+1)} = \mathbf{x}^{(k)} + \lambda_k \sum_i \frac{I_i - \langle \mathbf{a}_i, \mathbf{x}^{(k)} \rangle}{\|\mathbf{a}_i\|^2} \mathbf{a}_i \qquad (9)$$

where $\mathbf{a}_i$ is a vector with all the contributions of all the j basis functions onto the pixel i, and i goes over the selected image (different for each k). λ_k is a relaxation factor between 0 and 2.

The closer to 1 the faster the algorithm will converge, although this is only feasible if the experimental measurements are of good quality. In CryoEM, the Signal-to-Noise Ratio of the projections is in the order of 0.01. For this reason, λ is typically kept low.

Our output is the vector $\mathbf{x}_j$, that is, the Gaussian coefficients. By doing this, we are deconvolving the map with a Gaussian at the same time that we reconstruct it. In the multiresolution section below, we will show that the width of this Gaussian is locally defined and that we are, thus, doing a local deconvolution based on the local resolution of the map.

Zernike3D Algebraic Reconstruction Technique

One of the main reasons to choose ART as the basis for the ZART algorithm is the freedom it gives to supply prior knowledge during the reconstruction process. In the case of ZART, this information is related to the structural information of each particle, which is computed by the Zernike3D algorithm.

The Zernike3D method[26] is a novel approach able to describe per-particle conformational changes based on the estimation of a deformation field $\boldsymbol{g}_L$, so that the relationship between the deformed and the undeformed volume is

$$V_{\text{deformed}}(\mathbf{r}) = V_{\text{undeformed}}(\mathbf{r} + \boldsymbol{g}_L(\mathbf{r})) \qquad (10)$$

where the deformation field is expressed in terms of the Zernike3D basis $Z_{l,n,m}$ and a series of Zernike3D coefficients $\alpha_{l,n,m}$ as:

$$\boldsymbol{g}_L(\boldsymbol{r}) = \sum_{l=0}^{L} \sum_{n=0}^{N} \sum_{m=-l}^{l} \begin{pmatrix} \alpha_{l,n,m}^x \\ \alpha_{l,n,m}^y \\ \alpha_{l,n,m}^z \end{pmatrix} Z_{l,n,m}(\boldsymbol{r}) \qquad (11)$$

The estimation of the deformation field amounts to estimating the α coefficients in the equation

above. Once they are determined, we may use incorporate them in the series expansion to have a deformation, projection model (see Eq. 6):

$$I_{\text{deformed}}(\mathbf{s}) = \sum_j x_j G\left(\frac{(\mathbf{s}-\mathbf{s}_0)-E(\boldsymbol{r}_j+\boldsymbol{g}_L(\boldsymbol{r}_j))}{\sigma}\right) = \sum_j x_j a_{E,\mathbf{s}_0,\mathbf{g}_L,ij} \qquad (12)$$

That is, in the deformed projection, the coefficients of the undeformed map, x_j, have to be projected to a point given by the projection direction and the deformation field. The term $a_{E,\mathbf{s}_0,\mathbf{g}_L,ij}$ now encodes the projection, in-plane shift, and deformation.

The main advantage of including the heterogeneity information in the ART reconstruction process through the Zernike3D deformation fields is the possibility to properly correct the non-rigid alignments associated with macromolecular motions. In a normal reconstruction process, the reconstruction volume is assumed to be the conformational state represented by all the particles in the dataset. However, the previous assumption does not hold when the macromolecule exhibits large degrees of flexibility, leading to a motion-induced blurring in the resulting map. The per-particle deformation fields introduced a non-rigid alignment able to correct for the heterogeneity inconsistencies of the particles, making the dataset more consistent during the reconstruction process and thus reducing motion blur artefacts.

The unknowns of the linear equation system in Eq. 8, x_j, refer to the undeformed map. However, the A matrix contains projections of the deformed images. In this way, we obtain the remarkable result that ZART can reconstruct an undeformed map with information coming from the deformed particles together with the deformation field. Still, we should warn that since the calculation of the deformation field itself will never be perfect due to the image noise, errors in this estimation will translate into the "estimated" undeformed map; in other words, the quality of the reconstructed undeformed map depends on the capacity of the Zernikes to faithfully reproduce the observed deformations.

In order to improve the aspect of the final maps, ZART only uses the Gaussian convolution for the computation of the volume projections that will be compared to the experimental image. Once the correction image has been computed, ZART will look at the Gaussian coefficients to update the reconstruction. Since the Gaussian coefficients are sharper than the Gaussian itself, the reconstructed map will be sharper, making it easier to choose an appropriate threshold to visualize the reconstruction.

Regarding the CTF, particles should be previously corrected (for example, by means of a Wiener2D filter) before inputting them in ZART. The current criterion to stop iterations in ZART is

by reaching a maximum number of iterations specified by the user (by default, 10). Still, the user can decide whether to save or not the partial reconstructions for every iteration, in order to analyze how the reconstruction evolves and determine which iteration is yielding better results.

Multiresolution reconstruction

In addition, we have exploited the almost partition of unity property of Gaussians to propose a multiresolution reconstruction scheme. The resolution of the reconstructed map is limited by the standard deviation of the basis of the series expansion. Large standard deviations will lead to lower-resolution maps as we are introducing a stronger low-frequency component during the reconstruction. But, because the separation between bases is equal to the standard deviation, we will also require fewer coefficients and they will be less affected by noise.

Our multiresolution implementation discretizes the possible σ's to a finite set of possible values determined by the local resolution. Let us assume that we have M multiresolution levels, each one with a σ_m. Then, we have M superposing grids (at locations $\mathbf{r}_j^m$), and the series expansion above becomes:

$$V(\mathbf{r}) = \sum_m \left(\left(\sum_j x_j^m \delta \left(\mathbf{r} - \mathbf{r}_j^m \right) \right) \star b \left(\frac{\mathbf{r}}{\sigma_m} \right) \right) \qquad (13)$$

Our multiresolution reconstruction algorithm follows the next steps:

1. Initially, ZART performs two ART iterations to compute an initial even/odd reconstruction with the particles. At this moment, a large and fixed Gaussian spacing and standard deviation are used.
2. The two half maps are used to measure the current local resolution of the reconstruction with MonoRes.[19] We calculate the histogram of the local resolution and divide it into M equally populated bins. Then, we approximate the local resolution at the location $\mathbf{r}_j$ by the centre of its local resolution bin, let us refer to it as $\hat{R}(\mathbf{r}_j) = \hat{R}_m$. We associate a Gaussian standard deviation to each one of these bin centres:

$$\sigma_m = \frac{\hat{R}_m}{2T_s}$$

being T_s the sampling rate of the particles involved in the reconstruction. In this way, the Nyquist resolution corresponds to a value $\sigma = 1.0$, which defines the size of the Gaussian fulfilling the partition of unity.
3. Once the local standard deviations have been computed, ZART performs another two ART iterations in multiresolution mode. In our implementation, for each of the M grids, only the x_j^m coefficients of the series expansion whose local resolution is associated with σ_m are updated, while all the rest remain as 0.
4. Steps 2 and 3 are then repeated according to the total number of ART iterations specified by the user.
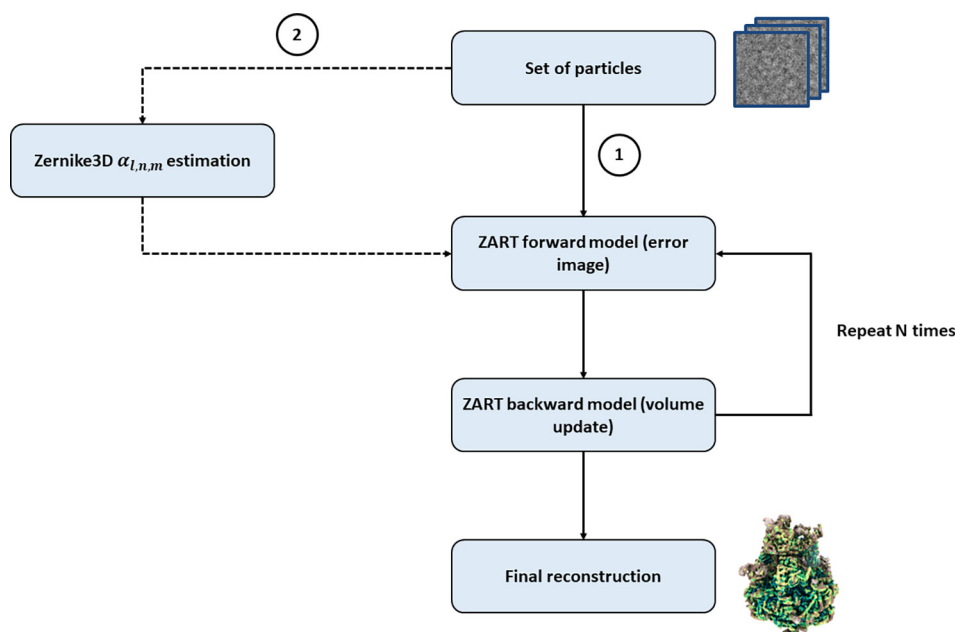

Figure 9. Diagram of the ZART reconstruction process in standard mode. (1) represents the steps followed when heterogeneity information is not available. (2) shows the motion blur correction workflow thanks to the estimation of the Zernike3D deformation fields for every particle in the dataset.
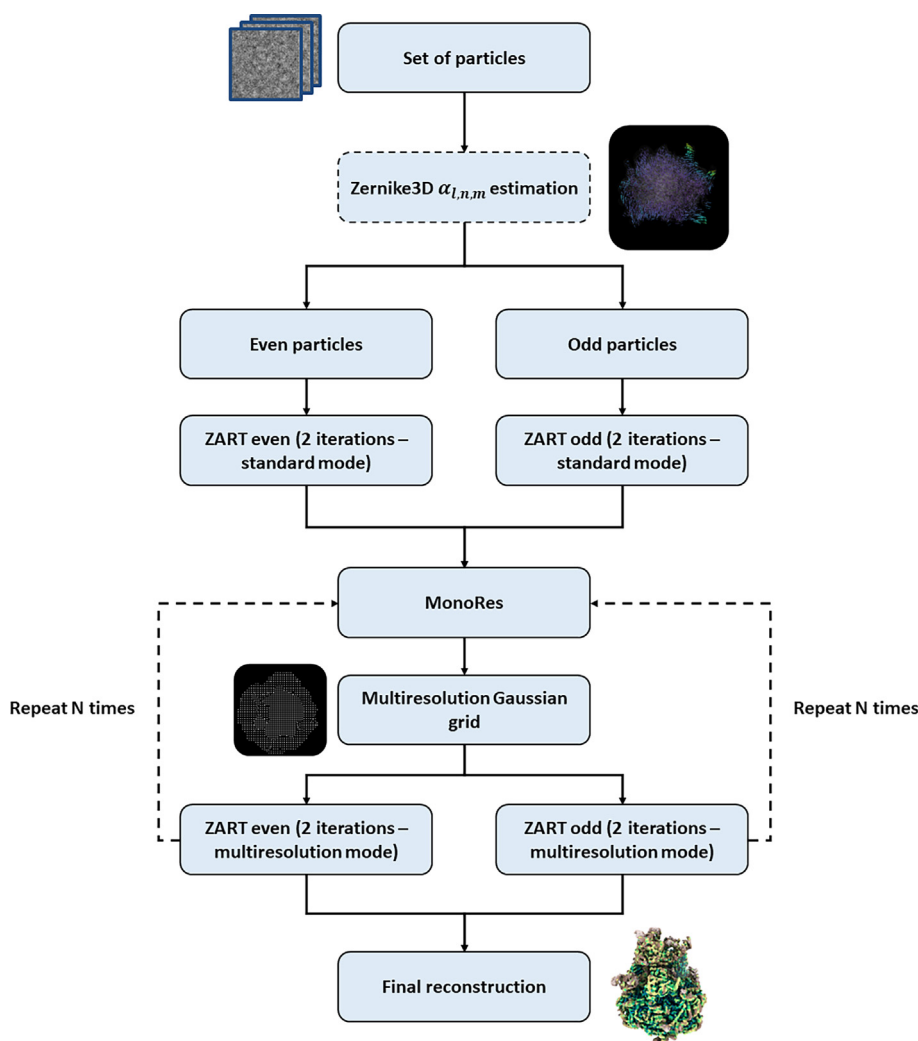
Figure 10. Diagram of the ZART reconstruction process in multiresolution mode. The estimation of the Zernike3D deformation fields is dotted, as it represents an optional step: if the estimation is computed, the multiresolution mode will reconstruct a motion blur-corrected version of the macromolecule.

When the multiresolution mode is selected, the user can determine the number of Gaussians (referred to as "levels" in the program) that will be used during the reconstruction (i.e. if $M = 3$ levels are chosen, the reconstruction will be able to use up to three Gaussians of different spacing and standard deviation).

A visual representation of the reconstruction process of both, standard and multiresolution modes is provided in Figure 9 and Figure 10.

Data Availability

The data used to test the ZART algorithm are publicly available in EMPIAR under the entries 10028 and 10391.

Code Availability

The ZART algorithm has been implemented in Xmipp[14] and it is available through Scipion 3.0[27] under the plugin `scipion-em-flexutils`.

CRediT authorship contribution statement

D. Herreros: Conceptualization, Methodology, Software, Validation, Writing – original draft. **J. Kiska:** Software. **E. Ramirez:** Resources. **J. Filipovic:** Software, Supervision. **J.M. Carazo:** Supervision, Writing – review & editing. **C.O.S. Sorzano:** Supervision, Writing – review & editing.

Competing Interests

The authors declare no competing interests.

Funding

Appendix A. Supplementary Data

Supplementary data associated with this article can be found, in the online version, at https://doi.org/10.1016/j.jmb.2023.168088.

References

1. Carroni, M., Saibil, H.R., (2016). Cryo electron microscopy to determine the structure of macromolecular complexes. *Methods* **95**, 78–85.
2. Scheres, S.H.W., Nuñez-Ramirez, R., Gomez-Yorente, Y., San Martin, C., Eggermont, P.P.B., Carazo, J.M., (2007). Modeling experimental image formation for likelihood-based classification of electron microscopy data. *Structure* **15** (10), 1167–1177.
3. Jin, Q., Sorzano, C.O.S., de la Rosa-Trevín, J.M., Bilbao-Castro, J.R., Núñez Ramírez, R., Llorca, O., Tama, F., Jonić, S., (2014). Iterative elastic 3D-to-2D alignment method using normal modes for studying structural dynamics of large macromolecular complexes. *Structure* **22**, 496–506.
4. Zhong, E.D., Bepler, T., Berger, B., Davis, J.H., (2021). Cryodrgn: reconstruction of heterogeneous cryo-em structures using neural networks. *Nat. Methods* **18**, 176–185.
5. Ludtke, S.J., Muyuan, C., (2021). Deep learning-based mixed-dimensional gaussian mixture model for characterizing variability in cryo-em. *Nat. Methods* **18**, 930–936.
6. Frank, J., Abbas, O., (2016). Continuous changes in structure mapped by manifold embedding of single-particle data in cryo-EM. *Methods* **100**, 61–67.
7. Punjani, A., Fleet, D.J., (2021). 3D flexible refinement: Structure and motion of flexible proteins from cryo-EM. *bioRxiv* **36**
8. Lederman, R.R., Anden, J., Singer, A., (2020). Hyper-molecules: on the representation and recovery of dynamical structures for applications in flexible macro-molecules in cryo-em. *Inverse Prob.* **36**
9. Sorzano, C.O.S., Vargas, J., Otón, J., Vilas, J.L., Kazemi, M., Melero, R., del Caño, L., Cuenca, J., et al., (2017). A survey of the use of iterative reconstruction algorithms in electron microscopy. *BioMed Res. Int.* **1–17**, 2017.
10. Herreros, D., Lederman, R.R., Krieger, J., Jiménez-Moreno, A., Martínez, M., Myška, D., Strelak, D., Filipovic, J., et al., (2023). Estimating conformational landscapes from Cryo-EM particles by 3D Zernike polynomials. *Nat. Commun.* **14**, 154.
11. Sorzano, C.O.S., Vargas, J., Otón, J., Abrishami, V., de la Rosa-Trevín, J.M., Fernández-Alderete, A., Martínez-Rey, C., Marabini, R., et al., (2015). Fast and accurate conversion of atomic models into electron density maps. *AIMS Biophys.* **2** (1), 8–20.
12. Wrapp, D., Wang, N., Corbett, K.S., Goldsmith, J.A., Hsieh, C., Abiona, O., Graham, B.S., McLellan, J.S., (2020). Cryo-em structure of the 2019-ncov spike in the prefusion conformation. *Science* **367** (6483), 1260–1263.
13. Abrishami, V., Bilbao-Castro, J.R., Vargas, J., Marabini, R., Carazo, J.M., Sorzano, C.O.S., (2015). A fast iterative convolution weighting approach for gridding-based direct Fourier three-dimensional reconstruction with correction for the contrast transfer function. *Ultramicroscopy* **157**, 79–87.
14. de la Rosa-Trevín, J.M., Otón, J., Marabini, R., Zaldívar, A., Vargas, J., Carazo, J.M., Sorzano, C.O.S., (2013). Xmipp 3.0: An improved software suite for image processing in electron microscopy. *J. Struct. Biol.* **184**, 321–328.
15. Tan, Y.Z., Zhang, L., Rodrigues, J., Zheng, R.B., Giacometti, S.I., Rosário, A.L., Kloss, B., Dandey, V.P., et al., (2020). Cryo-em structures and regulation of arabinofuranosyltransferase aftd from mycobacteria. *Molecular Cell* **78** (4), 683–699. al et..
16. Scheres, S.H.W., (2012). Relion: Implementation of a bayesian approach to cryo-em structure determination. *J. Struct. Biol.* **180**, 519–530.
17. Pettersen, E.F., Goddard, T.D., Huang, C.C., Meng, E.C., Couch, G.S., Croll, T.I., Morris, J.H., Ferrin, T.E., (2021). Ucsf chimerax: Structure visualization for researchers, educators, and developers. *Protein Sci.* **30** (1), 70–82.
18. Sanchez-Garcia, R., Gomez-Blanco, J., Cuervo, A., Carazo, J.M., Sorzano, C.O.S., (2021). Deepemhancer: a deep learning solution for cryo-em volume post-processing. *Commun. Biol.* **4**, 874.
19. Vilas, J.L., Gomez-Blanco, J., Conesa, P., Melero, R., de la Rosa-Trevin, J.M., Oton, J., Cuenca, J., Marabini, R., et al., (2018). Monores: Automatic and accurate estimation of local resolution for electron microscopy maps. *Structure* **26**, 337–344.

20. Wong, W., Bai, X., Brown, A., Fernandez, I.S., Hanssen, E., Condron, M., Tan, Y.H., Baum, J., et al., (2014). Cryo-em structure of the Plasmodium falciparum 80s ribosome bound to the anti-protozoan drug emetine. *eLife* **3**, e03080.

21. Punjani, A., Rubinstein, J.L., Fleet, D.J., Brubaker, M.A., (2017). cryoSPARC: algorithms for rapid unsupervised cryo-em structure determination. *Nat. Methods* **14**, 290–296.

22. Sorzano, C.O.S., Jiménez-Moreno, A., Maluenda, D., Martínez, M., Ramírez-Aportela, E., Krieger, J., Melero, R., Cuervo, A., et al., (2022). On bias, variance, overfitting, gold standard and consensus in single-particle analysis by cryo-electron microscopy. *Acta Crystall. Section D* **78** (4), 410–423.

23. Thevenaz, P., Ruttimann, U.E., Unser, M., (1998). A pyramid approach to subpixel registration based on intensity. *IEEE Trans. Image Process.* **7** (1), 27–41.

24. Bale, R., Grossman, J., Margrave, G., Lamoureux, M., (2002). Multidimensional partitions of unity and gaussian terrains. *CREWES Res. Report* **14**

25. Sorzano, C.O.S., Marabini, R., Vargas, J., Otón, J., Cuenca-Alba, J., Quintana, A., de la Rosa-Trevín, J.M., Carazo, J.M., (2014). Computational Methods for Three-Dimensional Microscopy Reconstruction, chapter Interchanging geometry information in electron microscopy single particle analysis: mathematical context for the development of a standard. Springer.

26. Herreros, D., Lederman, R.R., Krieger, J., Jiménez-Moreno, A., Martínez, M., Myška, D., Strelak, D., Filipovic, J., et al., (2021). Approximating deformation fields for the analysis of continuous heterogeneity of biological macromolecules by 3D Zernike polynomials. *IUCrJ* **8** (6), 992–1005.

27. de la Rosa-Trevín, J.M., Quintana, A., del Cano, L., Zaldívar, A., Foche, I., Gutiérrez, J., Gómez-Blanco, J., Burguet-Castell, J., et al., (2016). Scipion: A software framework toward integration, reproducibility and validation in 3D electron microscopy. *J. Struct. Biol.* **195** (1), 93–99.

a)

b)

	Mean	STD	Median	IQR [25,75]	Skewness
ZART MR (3L)	5.560189	2.647937	3.992471	4.421874	0.838478
CryoSparc Non-Uniform	6.515679	2.838180	5.351753	5.196824	0.472037
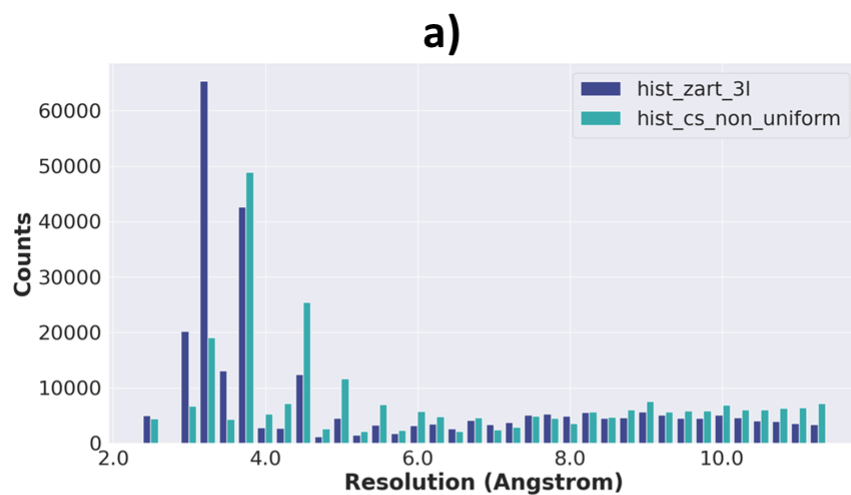
Suplemmentary Fig. 1: Local resolution statistics computed from the CryoSparc [1] non-uniform and ZART (multiresolution with no heterogeneity correction) reconstructions of the arabinofuranosyltransferase [2]. a) shows the local resolution histogram computed with MonoRes [3] using the reconstructed half maps. b) shows different histogram measurements drawn from the local resolution values. In this table, IQR stands for interquartile. Both results confirm that the multiresolution reconstruction of ZART pushes a larger number of voxels towards the high-resolution regime.
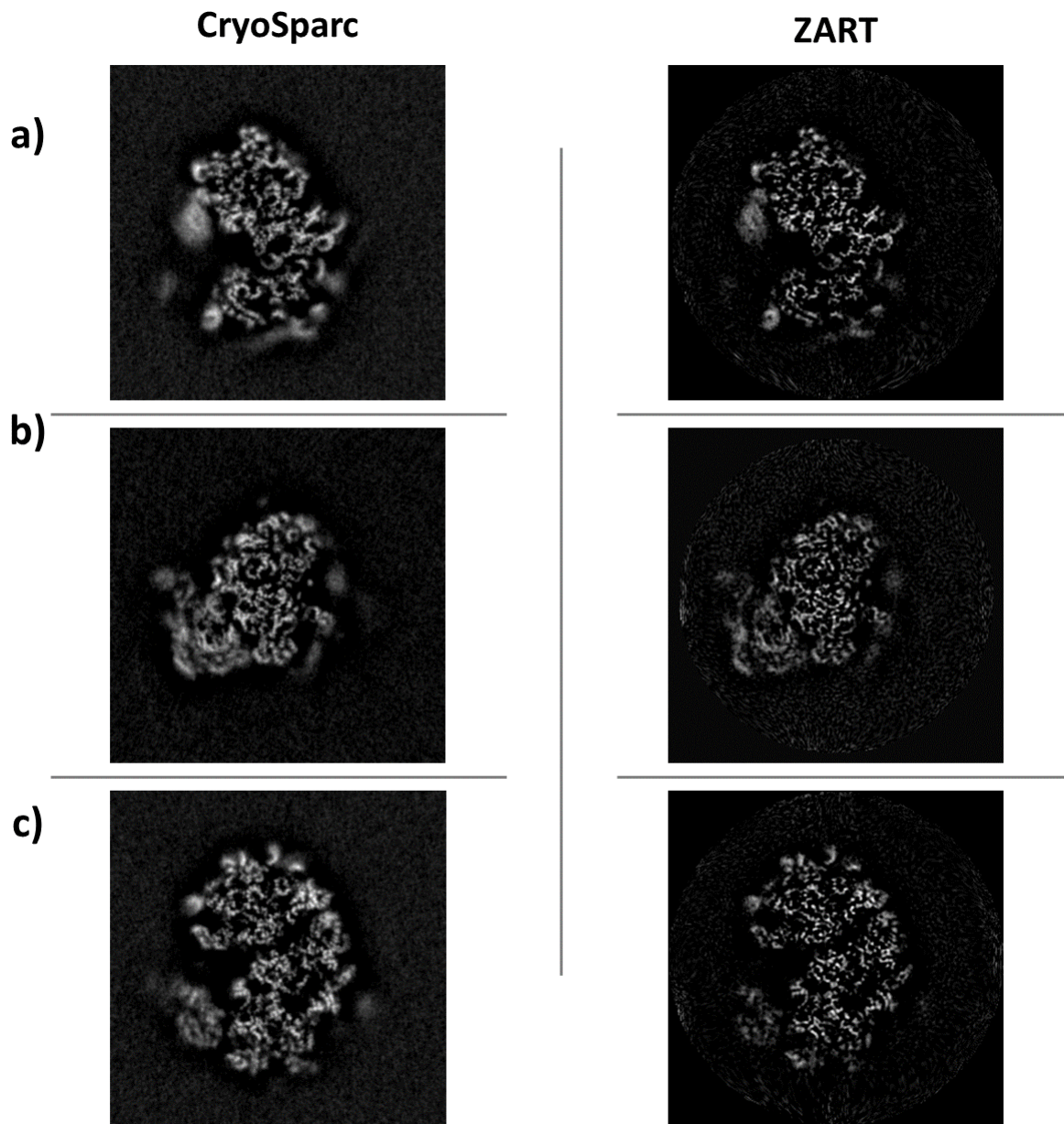
Suplemmentary Fig. 2: Comparison of several slices of CryoSparc [1] and ZART (with heterogeneity correction applied). In the EMPIAR-10028 [4] dataset, the small subunit of the ribosome has a larger degree of flexibility, leading to a motion-induced blur as shown in the CryoSparc slices. Our ZART approach produces a more detailed reconstruction of this region thanks to the application of the Zernike3D [5] deformation fields during the reconstruction process. In addition, the intrinsic sharpening of ZART leads to a better representation of the overall signal.

References

[1] A. Punjani, J.L. Rubinstein, D.J. Fleet, and M.A. Brubaker. cryoSPARC: algorithms for rapid unsupervised cryo-em structure determination. *Nature Methods*, 14:290–296, 2017.

[2] Y.Z. Tan, L. Zhang, J. Rodrigues, R.B. Zheng, S.I. Giacometti, A.L. Rosário, B. Kloss, V.P. Dandey, H. Wei, R. Brunton, and al et. Cryo-em structures and regulation of arabinofuranosyltransferase aftd from mycobacteria. *Molecular cell*, 78(4):683–699, 2020.

[3] J.L. Vilas, J. Gomez-Blanco, P. Conesa, R. Melero, J.M. de la Rosa-Trevin, J. Oton, J. Cuenca, R. Marabini, J.M. Carazo, and C.O.S. Sorzano. Monores: Automatic and accurate estimation of local resolution for electron microscopy maps. *Structure*, 26:337–344, 2018.

[4] W. Wong, X. Bai, A. Brown, I.S. Fernandez, E. Hanssen, M. Condron, Y.H. Tan, J. Baum, and S.H.W. Scheres. Cryo-em structure of the *Plasmodium falciparum* 80s ribosome bound to the anti-protozoan drug emetine. *eLife*, 3:e03080, 2014.

[5] D. Herreros, R.R. Lederman, J. Krieger, A. Jiménez-Moreno, M. Martínez, D. Myška, D. Strelak, J. Filipovic, C.O.S. Sorzano and J.M. Carazo. Estimating conformational landscapes from Cryo-EM particles by 3D Zernike polynomials. *Nature Communications*, 14:154, 2023.